Activating Grain Boundaries in Hybrid Perovskite Solar Cells

Bin Yang,[1] Ondrej Dyck,[2] Jonathan Poplawsky,[1] Jong Keum,[1] Alexander Puretzky,[1]

Sanjib Das,[3] Ilia Ivanov,[1] Christopher Rouleau,[1] Gerd Duscher,[2]

David Geohegan,[1] Kai Xiao[1]*

[1]Center for Nanophase Materials Sciences, Oak Ridge National Laboratory, Oak Ridge, TN, 37831, USA.

[2]Department of Materials Science and Engineering, University of Tennessee, Knoxville, TN, 37996, USA.

[3]Department of Electrical Engineering and Computer Science, University of Tennessee, Knoxville, TN, 37996, USA.

*To whom correspondence should be addressed. Email: xiaok@ornl.gov

Notice: This manuscript has been authored by UT-Battelle, LLC, under Contract No. DE-AC05-00OR22725 with the U.S. Department of Energy. The United States Government retains and the publisher, by accepting the article for publication, acknowledges that the United States Government retains a non-exclusive, paid-up, irrevocable, world-wide license to publish or reproduce the published form of this manuscript, or allow others to do so, for United States Government purposes.

Activating Grain Boundaries in Hybrid Perovskite Solar Cells

Bin Yang,[1] Ondrej Dyck,[2] Jonathan Poplawsky,[1] Jong Keum,[1] Alexander Puretzky,[1]

Sanjib Das,[3] Ilia Ivanov,[1] Christopher Rouleau,[1] Gerd Duscher,[2]

David Geohegan,[1] Kai Xiao[1]*

[1]Center for Nanophase Materials Sciences, Oak Ridge National Laboratory, Oak Ridge, TN, 37831, USA.

[2]Department of Materials Science and Engineering, University of Tennessee, Knoxville, TN, 37996, USA.

[3]Department of Electrical Engineering and Computer Science, University of Tennessee, Knoxville, TN, 37996, USA.

*Correspondence to: xiaok@ornl.gov

Abstract: Grain boundaries (GBs) in hybrid organic-inorganic perovskite solar cells are controversial, thought to be either benign, or detrimental locations for non-radiative carrier recombination that decrease device power conversion efficiency (PCE). Here, electron beam induced current imaging unambiguously establishes that grain boundaries in methylammonium lead tri-iodide ($CH_3NH_3PbI_3$) thin film solar cells are intrinsically detrimental, but can be activated to enhance efficiencies. A simple layer-by-layer solution casting and post annealing process is reported to grow perovskite films with large, vertically-oriented single-crystalline grains. The hole-transport medium Spiro-OMeTAD is infiltrated into the vertical GBs to form a bulk heterojunction, activating the GBs for increased carrier collection efficiency by inducing space-charge-regions that suppress non-radiative recombination. Active-GB solar cells yielded average PCE of 16.3±0.9%, comparable to the best solution-processed perovskite devices, establishing them as important alternatives to growing ideal single crystal films in the pursuit toward theoretical maximum PCE with industrially realistic processing techniques.

One Sentence Summary: A bulk heterojunction perovskite solar cell with single-crystalline grains and activated grain boundaries is shown to increase carrier collection for high efficiencies.

Main Text: Organometal halide perovskites exhibit great promise for low-cost and high-efficiency solar cells due to the relative ease through solution casting(*1-3*) to achieve high degrees of crystallinity,(*4*) excellent carrier transport properties,(*5*) tunable optical bandgaps,(*6, 7*) and strong light absorption.(*8, 9*) Grain boundary (GB) losses have plagued polycrystalline solar cells for several decades, where defects, traps as well as energetic disorder cause significant non-radiative recombination energy loss and strongly limit achievable power conversion efficiencies (PCEs).(*7, 10*) The role of GBs in polycrystalline hybrid perovskite thin films is still under intensive debate.(*7, 11-16*) Theoretical studies predict that the GBs are intrinsically benign in perovskites,(*13, 15*) however, recent works propose that the primary energy loss in hybrid perovskite solar cells is caused by non-radiative recombination of carriers due to deep trap states at grain boundaries (GBs) and point defects, such as interstitial defects or vacancies, in the perovskite crystal lattice.(*11, 14, 16, 17*) Therefore, overcoming non-radiative recombination in perovskite thin films has concentrated on obtaining large crystallites within films, with low densities of GBs and intragranular defects,(*16, 18*) as well as on passivating the GB defect states.(*11, 17*) Ideally, growth of single crystal perovskite films would completely remove GBs to suppress energetic disorder and non-radiative recombination losses, to enable organometal halide perovskite photovoltaics with PCE approaching the theoretical Shockley-Queisser maxima of ~30%.(*19*) In practice, however, growth of single crystal perovskite films, such as methylammonium lead tri-iodide ($CH_3NH_3PbI_3$), is challenging using single-step processing due to the fast chemical reaction between lead iodide (PbI_2) and methylammonium iodide (CH_3NH_3I) precursors that produces a large quantity of stable $CH_3NH_3PbI_3$ seed clusters.(*8*) These seed

clusters tend to nucleate multiple grains during the crystallization process, making it very difficult to achieve single crystal perovskite films. In addition, mesoporous titanium dioxide (TiO_2) scaffold structures that are widely-used also force high a density of GBs by limiting the size of perovskite crystal grains within confined dimensions.

In this work, rather attempting to passivate or eliminate GBs, an alternative approach is introduced. Vertical boundaries between large single-crystalline perovskite grains are first formed through a simple processing and annealing treatment, and then activated by introducing a space-charge-region (SCR) in order to significantly reduce non-radiative recombination losses to significantly enhance carrier collection. The resulting device represents a new type of bulk heterojunction (BHJ) structure comprised of large, single-crystalline perovskite grains and vertically-aligned GBs infiltrated with p-type doped 2′-7,7′-tetrakis(N,Ndi-p-methoxyphenylamine)-9,9-spirobifluorene (Spiro-OMeTAD). The average PCE of the devices with this structure are 16.3±0.9% with a near-unity photogenerated carrier collection efficiency, which are among the best low-temperature, solution-processed $CH_3NH_3PbI_3$ solar cells.

The GB activation mechanism is presented in Fig. 1A-B. For regular polycrystalline perovskite films with a high-density of randomly-oriented GBs, the defect-ridden GBs scatter or trap the photogenerated carriers causing recombination and energy loss (Fig. 1A). In order to activate the GBs, a new type of microstructured perovskite film is proposed, one that has large single-crystal grains and vertically-aligned GBs across the entire film as shown in Fig. 1B. For such structures, the normally-detrimental GBs are activated to act as carrier collection channels through the diffusion of Spiro-OMeTAD molecules along these GBs to penetrate the perovskite film thickness. Heterojunctions created between the single-crystal grains and the Spiro-OMeTAD-filled-GBs-channels lead to SCRs in the vicinity of the GBs allowing significantly

more photogenerated holes, particularly holes generated on the bottom side of the perovskite film, to be extracted through the Spiro-OMeTAD filled GBs, while the separated electrons drift toward the compact TiO_2 layer.

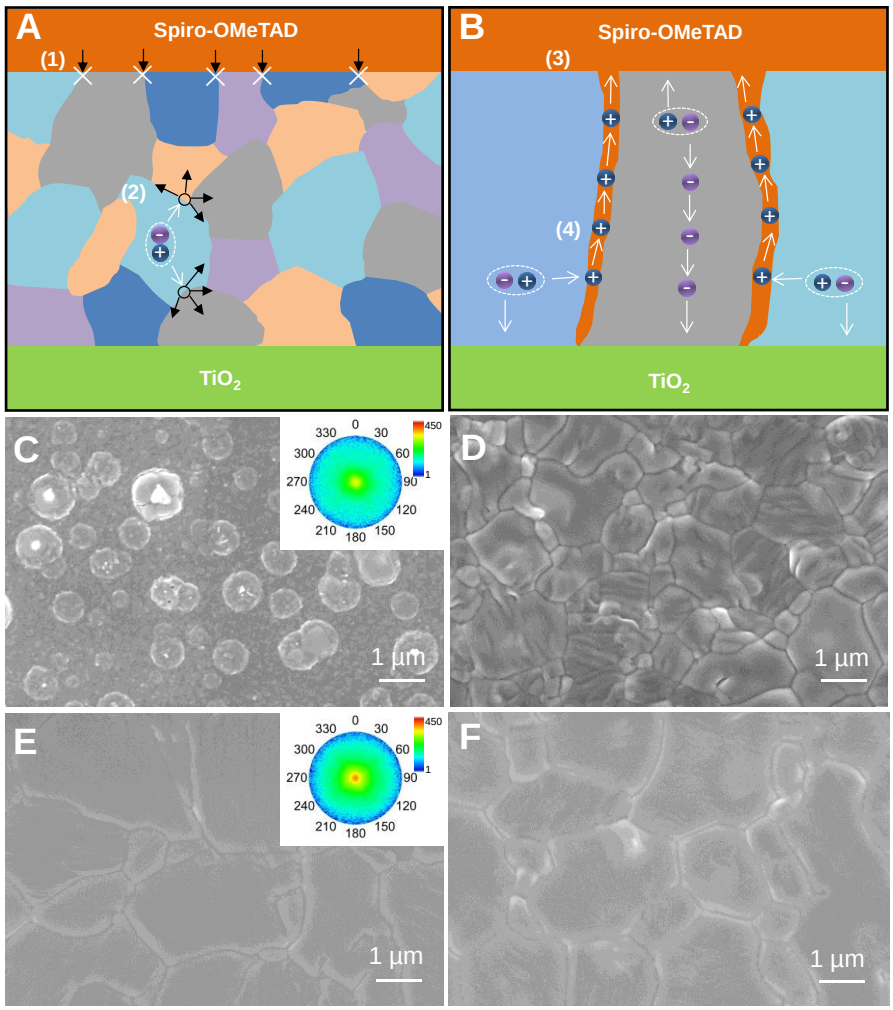

Fig. 1. Activating grain boundary mechanism. (A) Regular polycrystalline perovskite film has small grains and randomly-aligned GBs: (1) the deep infiltration of Spiro-OMeTAD into GBs is difficult, (2) photogenerated carriers are scattered or trapped at GBs. (B) The proposed microstructure perovskite film has large single crystal grains and vertically-aligned GBs across the entire film: (3) deep infiltration of Spiro-OMeTAD material (orange color) into GBs, (4) extraction of holes generated at the bottom side of the perovskite film through active GB channels, while the left-behind electrons travel toward the compact TiO_2 layer. Different colors indicate different orientations of grains in a perovskite film. SEM images show the crystal growth with respect to the thermal-annealing time: (C) air-exposure-only, (D) 60 minutes anneal, (E) 120 minutes anneal, and (F) 180 minutes anneal. Inset of (C) and (E) show the corresponding X-ray pole figures for the (110) plane of the $CH_3NH_3PbI_3$ crystal, which were measured at 2θ of 14.05°.

Layer-by-layer spin-coated PbI_2/CH_3NH_3I bilayer films were initially exposed in ambient air (humidity of ~30%) to introduce moisture during the chemical formation of the perovskite layers (Fig. S1). In fact, the spin-coated PbI_2/CH_3NH_3I bilayer film completely converts into a polycrystalline perovskite film after air-exposure for 60 minutes, as shown by the gradual disappearance of the PbI_2 Bragg peak at 12.56° and synchronous enhancement of the $CH_3NH_3PbI_3$ Bragg peak at 14.05° with respect to exposure time (Fig. S2-3). This result indicates that thermal-annealing is not necessary to drive the interdiffusion between the PbI_2 and CH_3NH_3I layers. It also reveals that moisture can be another driving force to promote such interdiffusion and perovskite crystallization to increase grain size (Fig. S4), which may be due to formation of a more reactive intermediate phase $CH_3NH_3PbI_3{\cdot}H_2O$.(*2*, *20*) The X-ray pole figures were used to probe the global orientation and crystallographic texture of the perovskite crystals, which clearly indicate that the air-exposure-only $CH_3NH_3PbI_3$ perovskite films already form well-oriented perovskite films, as suggested by a maxima orientation of [110] (inset of Fig. 1C). This is significant because grains with the same orientation generally require less energy to coalesce than those with different orientations, leading to larger crystal grains and a lower density of GBs.(*21*) Thermal-annealing at 100 °C in an N_2-filled glovebox was further applied to coalesce the smaller grains (107.5±1.8 nm, as shown in Fig. 1C and Fig. S3), which grew to ~2 μm in the lateral direction after annealing for 120 minutes (Fig. 1D-F). The annealed perovskite film exhibited a much better texture than the air-exposure-only perovskite film, as shown in the inset of Fig. 1E.

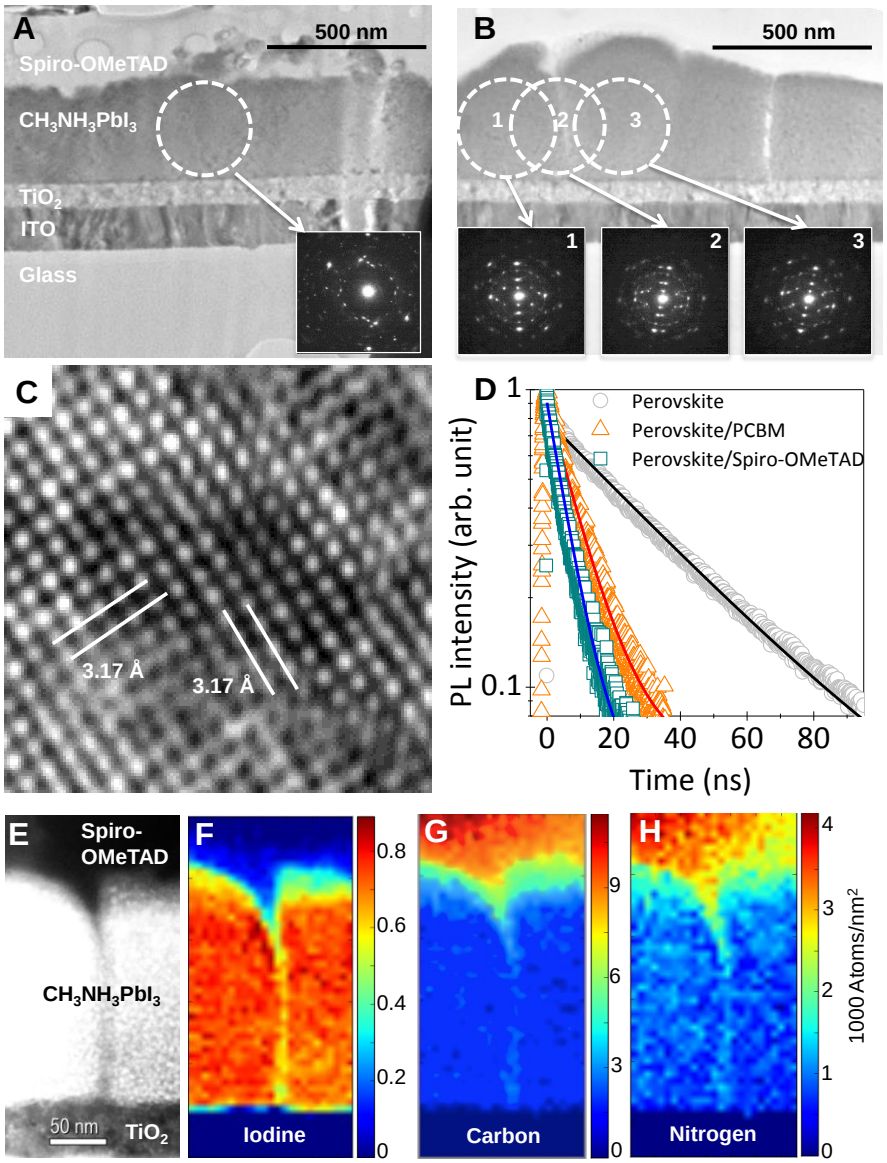

Fig. 2. Infiltration of Spiro-OMeTAD into grain boundaries. The cross-sectional bright field TEM images show vertical phase morphologies: air-exposure-only (A), and 120 minutes-anneal (B). The inset of (A) and (B) shows the corresponding SAED patterns to demonstrate primary polycrystalline phase and large single crystal grains in (A) and (B), respectively. (C) An atomic resolution TEM image acquired from a $CH_3NH_3PbI_3$ film (B). (D) Transient photoluminescence spectroscopy curves were obtained from a 120 minutes-annealed $CH_3NH_3PbI_3$ films at 760±6 nm with excitation of 400 nm. Time-resolved photoluminescence spectroscopy (dotted curves) fitted by a single exponential decay (solid lines). A Z-contrast dark-field STEM image (E) and EELS maps (F-H) demonstrate a GB infiltrated with Spiro-OMeTAD between two $CH_3NH_3PbI_3$ grains. The atomic areal density elemental maps (F, iodine; G, carbon; and H, nitrogen) show significant rich content of both carbon and nitrogen and lack of iodine in GBs.

To investigate the detailed microstructure of the perovskite film in the devices, transmission electron microscopy (TEM) was applied to image the cross-sectional morphology of the entire device with architecture (ITO/TiO_2/$CH_3NH_3PbI_3$/Spiro-OMeTAD/Ag). As for the air-exposure-only $CH_3NH_3PbI_3$ film, small crystalline grains with polycrystalline features are shown by a TEM image and selected area electron diffraction (SAED) patterns with random diffraction spots in Fig. 2A. With regard to the annealed $CH_3NH_3PbI_3$ film, large-oriented crystalline grains and vertically-aligned GBs were clearly identified (Fig. 2B). Similar crystallographic orientations along the direction parallel to the glass substrate were observed, as shown by two typical SAED patterns acquired in adjacent grains (patterns 1 and pattern 3); Pattern 2 is superposition of patterns 1 and 3 as the SAED was taken across the GB (Fig. 2B). The lateral size of typical single crystal domains exceeded our aperture size of 300 nm, which easily illuminated single crystal regions. To investigate the vertical crystal grain size, a smaller SAED aperture with 180 nm diameter was inserted and used to acquire a series of similar SAED patterns perpendicular to the film substrate through the entire ~450 nm-thick perovskite layer (Fig. S5). The results suggest that a single crystal domain crosses the entire film in the perpendicular direction. Atomic resolution TEM images show a clear lattice fringes indicating the formation of a crystalline structure with a lattice spacing of 3.17 Å, which could be indexed as (220) of the tetragonal $CH_3NH_3PbI_3$ phase (Fig. 2C, Fig. S6).(*22*) This was further confirmed by the XRD patterns (Fig. S2). The excellent crystallinity results in a two times longer electron- and hole-diffusion lengths (171 nm and 225 nm, respectively, as shown in Fig. S7) compared to those in the one-step, spin-coated $CH_3NH_3PbI_3$ films, as revealed by time-resolved photoluminescence (PL) spectroscopy measurements (Fig. 2D).(*23, 24*)

In order to understand how infiltration of Spiro-OMeTAD in the GBs between these vertically-aligned single-crystalline grains form bulk heterojunctions, the cross-sectional morphology of the $CH_3NH_3PbI_3$ films were examined with Z-contrast scanning transmission electron microscopy (Z-STEM) and electron energy loss spectroscopy (EELS). The annealed perovskite films have vertically-aligned GBs as shown in the dark field image (Fig. 2E), which may be due to the creep of GBs and coalescence of small grains. In order to reveal the material in the GBs, corresponding EELS map images of iodine (Fig. 2F), carbon (Fig. 2G), and nitrogen (Fig. 2H) atomic areal density were acquired (a highly-magnified GB map is shown in Fig. S8). The lack of iodine indicates the absence of $CH_3NH_3PbI_3$, CH_3NH_3I, and PbI_2 precursors, while the rich content of both C and N unambiguously shows the presence of Spiro-OMeTAD infiltrated in the boundaries between the perovskite grains. It should be noted that the direct contact of Spiro-OMeTAD with TiO_2 does not short circuit the device due to the formation of high Schottky barrier between Spiro-OMeTAD with TiO_2.(*25, 26*)

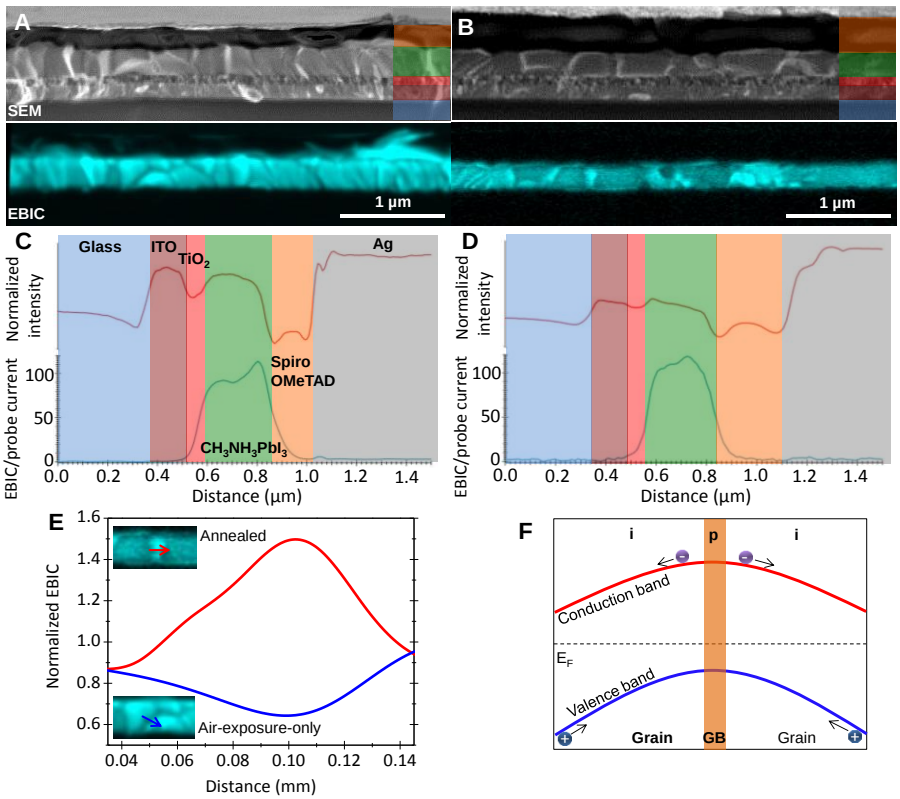

Fig. 3. Grain boundaries as active carrier collection channels. Cross-sectional SEM image (up) and corresponding EBIC image (down) of two devices: air-exposure-only (A), and 120 minutes-anneal (B). The corresponding line profiles of the cross-sectional SEM image (up, red curve) and EBIC image (down, green curve) at the indicated regions as shown insets: (C) air-exposure-only, and (D) 120 minutes-anneal. A gain of 1E6 V/A and 1E7 V/A were used for the annealed and air-exposure-only samples, respectively. This explains the relatively noisier EBIC image for the annealed sample (B) compared to the air-exposure-only sample (A). Although the image is noisier, the overall measured EBIC current/probe current ratio was very similar for both samples, as seen in (C, D). (E) Normalized line profiles of EBIC current across the GBs between two $CH_3NH_3PbI_3$ grains in the air-exposure-only (blue arrow and blue solid line) and 120 minutes-annealed (red arrow and red solid line) perovskite photovoltaics. (F) Energy band diagram across a GB schematically showing the separation of electron-hole pairs in space charge region in vicinity of GBs. The holes drift toward the GBs, while electrons drift away from the GBs.

Electron beam induced current (EBIC) measurements were applied to further reveal the suppression of recombination and enhanced carrier collection in the vicinity of the GBs. In EBIC, highly-energetic electrons are used to generate several electron-hole pairs in targeted areas of a semiconductor, which are separated due to internal electric fields and collected to attached electrodes. By scanning the electron beam, EBIC measurements pictorially reveal the

presence of internal electric fields, minority carrier diffusion lengths, and the location of p-n junctions at the mesoscopic scale.(*27*) EBIC scans were performed for devices fabricated by air-exposure-only (Fig. 3A, C) and after annealing (Fig. 3B, D). It is clear from these data that electrical current is generated throughout the entire perovskite active layer, which is indicative of p-i-n structures within both devices.(*12*) As shown in Fig. 3E and Fig. S9, the EBIC signal is weaker in the GBs than inside grains for the air-exposure-only polycrystalline perovskite film devices, which indicates the presence of recombination due to the high density of defects in the GBs, such as point defects and dangling bonds. This result reveals that GBs in perovskite films are not intrinsically benign which is contrary to theoretical predictions.(*13, 15*) However in the annealed perovskite device, a higher EBIC current was measured in the vicinity of the GB with respect to the surrounding grains, which implies that the GBs are acting as active channels for electrical current flow rather than strong recombination regions. As shown in the schematic energy band diagram across a GB (Fig. 3F), the enhancement in carrier collection is ascribed to a BHJ between perovskite grains and p-type doped Spiro-OMeTAD filled GBs. The SCRs between the $CH_3NH_3PbI_3$ grains separate photogenerated electron-hole pairs,(*27*) and allow the electrons and holes to drift toward the two respective electrodes. Spiro-OMeTAD filled GBs are good pathways for holes to travel with less resistance to the device back contact. Since the electron mobility is twice the hole mobility in $CH_3NH_3PbI_3$ perovskite films,(*28*) under the internal electric field the holes should drift much slower toward the Spiro-OMeTAD layer compared to the electrons as they travel to the TiO_2 layer. Therefore, the proposed microstructured perovskite film devices have dual functions of (1) activating detrimental GBs, and (2) balancing electron and hole collection.

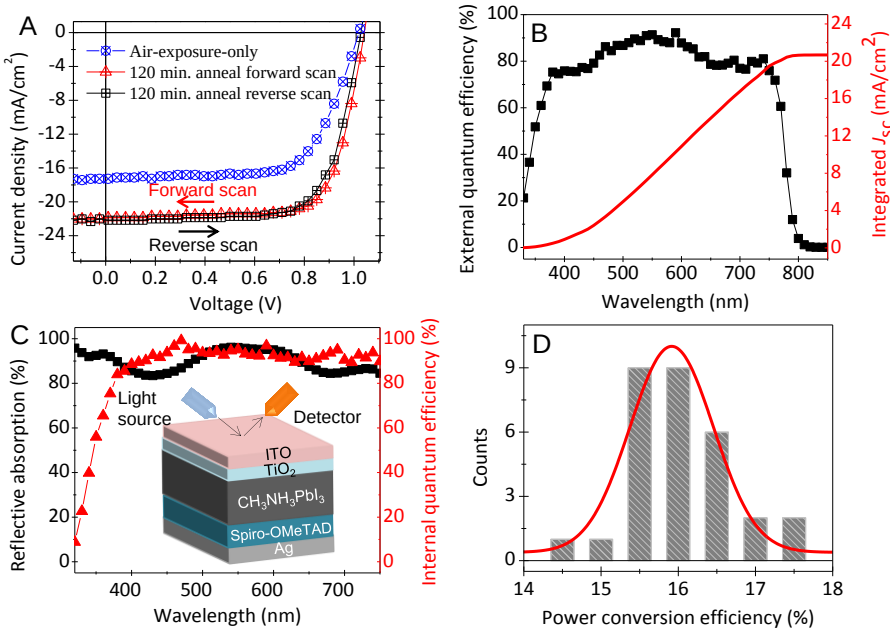

Fig. 4. Device performance. (A) *J-V* curves of devices based on air-exposure-only perovskite film (blue triangle curve), and 120 minutes-annealed perovskite film: forward scan (red triangle curve) and reverse scan (black square curve). Forward and reverse scan *J-V* curves show negligible hysteresis loop. (B) External quantum efficiency (EQE) as a function of wavelength (black square curve), and integrated short circuit current density (J_{SC}) (red curve). (C) Reflective absorption (black square curve) and calculated internal quantum efficiency (IQE, red triangle curve) as a function of wavelength, and the inset shows the reflective absorption measurement setup. (D) A Gaussian distribution of the device efficiencies based on ~30 devices.

The device in Fig. 4A, based on an air-exposure-only $CH_3NH_3PbI_3$ perovskite film, exhibits high performance with a short-circuit current density (J_{SC}) of 17.28 mA/cm^2, an open circuit voltage (V_{OC}) of 1.02 V, a fill factor (*FF*) of 66.9 %, and a PCE of 11.8 %. Further thermal-annealing the air-exposure-perovskite film can significantly enhance the photovoltaic performance (Fig. S10, Table S1). The typical device with 120 minutes-annealed perovskite film yielded a J_{SC} of 21.9 mA/cm^2, V_{OC} of 1.041 V, *FF* of 73.5%, and *PCE* of 16.8% (Fig. 4A). The significant enhancement in *PCE* is due to a notably improved light absorption (Fig. S11), suppressed non-radiative carrier recombination at GBs, and enhanced carrier collection.(*14*) Negligible differences between the *J-V* curves were observed in this annealed perovskite film

device when comparing the forward-to-reverse sweep and reverse-to-forward sweep, which may be attributed to the infiltrated Spiro-OMeTAD draining out the accumulated carriers at GBs.(*17*) In order to examine the measured J_{SC} from the *J-V* sweep, the external quantum efficiencies (EQEs) of the devices were also measured, with a value of ~90% at 580 nm (Fig. 4B). The *EQE* spectrum integration over the AM 1.5 G solar spectrum (100 mW/cm^2), yields a J_{SC} of 20.7 mA/cm^2, which is ~5% smaller than the J_{SC} obtained from *J-V* sweep. Such a small discrepancy may be caused by instability of the oxidized Spiro-OMeTAD.(*29*) The absorption spectrum was measured in reflectance, mimicking the light absorption process in real devices, as depicted in the inset of Fig. 4C. The internal quantum efficiency (IQE), calculated by dividing the EQE by the reflective absorption, is ~95% throughout the entire visible spectrum from 400 nm to 700 nm (Fig. 4C), which indicates remarkably efficient charge carrier generation and collection. Fig. 4D shows a Gaussian distribution of the device efficiencies based on over 30 devices, with a mean *PCE* of 16.3±0.9%. Therefore, compared to the challenging growth of $CH_3NH_3PbI_3$ single crystal films, vertically-oriented single-crystal grains with active-GBs acting as bulk heterojunctions present a facile and important alternative pathway to achieve the theoretical maximum PCE in perovskite solar cells.

References and notes

1. P. Docampo *et al.*, *Nat. commun.* **4**, 2761 (2013).
2. H. Zhou *et al.*, *Science* **345**, 542-546 (2014).
3. A. Mei *et al.*, *Science* **345**, 295-298 (2014).
4. M. Liu *et al.*, *Nature* **501**, 395-398 (2013).
5. C. Kagan *et al.*, *Science* **286**, 945-947 (1999).
6. F. Hao *et al.*, *Nat. Photonics* **8**, 489-494 (2014).
7. M. A. Green *et al.*, *Nat. Photonics* **8**, 506-514 (2014).
8. J. Burschka *et al.*, *Nature* **499**, 316-319 (2013).
9. N. J. Jeon *et al.*, *Nat. Mater.* **13**, 897–903 (2014).
10. T. DiStefano *et al.*, *Appl. Phys. Lett.* **30**, 351-353 (1977).
11. A. Abate *et al.*, *Nano letters* **14**, 3247–3254 (2014).
12. E. Edri *et al.*, *Nat. commun.* **5**, 3461 (2014).

13. J. Kim *et al.*, *J. Phys. Chem. Lett.* **5**, 1312-1317 (2014).
14. W. Tress *et al.*, *Adv. Energy Mater.*, 1400812 (2014).
15. W. J. Yin *et al.*, *Adv. Mater.* **26**, 4653-4658 (2014).
16. D. Zhao *et al.*, *Adv. Energy Mater.*, 1401855 (2014).
17. Y. Shao *et al.*, *Nat. Commun.* **5**, 5784 (2014).
18. J.-H. Im *et al.*, *Nature Nanotech.* **9**, 927–932 (2014).
19. W. Shockley *et al.*, *J. Appl. Phys.* **32**, 510-519 (1961).
20. F. Hao *et al.*, *J. Am. Chem. Soc.* **136**, 16411–16419 (2014).
21. L. Wang *et al.*, *Nat. commun.* **5**, 4402 (2014).
22. T. Baikie *et al.*, *J. Mater. Chem. A* **1**, 5628-5641 (2013).
23. S. D. Stranks *et al.*, *Science* **342**, 341-344 (2013).
24. G. Xing *et al.*, *Science* **342**, 344-347 (2013).
25. J. Krüger *et al.*, *Appl. Phys. Lett.* **79**, 2085-2087 (2001).
26. U. Bach *et al.*, *Nature* **395**, 583-585 (1998).
27. C. Li *et al.*, *Phys. Rev. Lett.* **112**, 156103 (2014).
28. C. S. Ponseca Jr *et al.*, *J. Am. Chem. Soc.* **136**, 5189-5192 (2014).
29. W. H. Nguyen *et al.*, *J. Am. Chem. Soc.* **136**, 10996-11001 (2014).

Acknowledgements

This research was conducted at the Center for Nanophase Materials Sciences (CNMS), which is a DOE Office of Science User Facility.